



Characterizing and correcting phase biases in short-term, multilooked interferograms

Yasser Maghsoudi^{a,*}, Andrew J. Hooper^a, Tim J. Wright^a, Milan Lazecky^a, Homa Ansari^b

^a COMET, School of Earth and Environment, University of Leeds, LS2 9JT, UK

^b Remote Sensing Technology Institute (IMF), German Aerospace Center (DLR), Germany

ARTICLE INFO

Editor: Jing M. Chen

Keywords:

InSAR
Phase bias
Fading signal
Correction

ABSTRACT

Interferometric Synthetic Aperture Radar (InSAR) is widely used to measure deformation of the Earth's surface over large areas and long time periods. A common strategy to overcome coherence loss in long-term interferograms is to use multiple multilooked shorter interferograms, which can cover the same time period but maintain coherence. However, it has recently been shown that using this strategy can introduce a bias (also referred to as a “fading signal”) in the interferometric phase. We isolate the signature of the phase bias by constructing “daisy chain” sums of short-term interferograms of different length covering identical 1-year time intervals. This shows that the shorter interferograms are more affected by this phenomenon and the degree of the effect depends on ground cover types; cropland and forested pixels have significantly larger bias than urban pixels and the bias for cropland mimics subsidence throughout the year, whereas forests mimics subsidence in the spring and heave in the autumn. We, propose a method for correcting the phase bias, based on the assumption, borne out by our observations, that the bias in an interferogram is linearly related to the sum of the bias in shorter interferograms spanning the same time. We tested the algorithm over a study area in western Turkey by comparing average velocities against results from a phase linking approach, which estimates the single primary phases from all the interferometric pairs, and has been shown to be almost insensitive to the phase bias. Our corrected velocities agree well with those from a phase linking approach. Our approach can be applied to global compilations of short-term interferograms and provides accurate long-term velocity estimation without a requirement for coherence in long-term interferograms.

1. Introduction

Interferometric Synthetic Aperture Radar (InSAR) is a powerful tool for monitoring ground deformation associated with earthquakes, volcanoes, landslides, and anthropogenic activities (e.g. Biggs et al., 2009; Foroughnia et al., 2019; Juncu et al., 2017; Massonnet et al., 1995; Temtime et al., 2018; Walters et al., 2011; Weiss et al., 2020). On a first order, the accuracy of the estimated deformation is thought to depend on uncorrected tropospheric and ionospheric delays, errors in phase unwrapping, uncertainties in knowledge of satellite position, phase decorrelation due to changes in scattering behavior between successive images, and system noise. Most of these error terms are associated with individual epochs and cancel out when calculating the wrapped loop closure phase at full spatial resolution, $\Delta\varphi$, defined for three epochs (i, j, k) as:

$$\Delta\varphi_{i,k} = |\varphi_{i,k} - (\varphi_{i,j} + \varphi_{j,k})|_{2\pi} \quad (1)$$

where $\varphi_{i,j}$, for example, is the phase difference for a pixel in the interferogram between epochs i and j , and $||_{2\pi}$ indicates that the result is given modulo 2π (i.e. wrapped) (Michaelides et al., 2019; Zwieback et al., 2016).

For full-resolution processing, the wrapped loop closure phase must be zero. If multilooking, or other forms of spatial filtering, is carried out as part of the processing, then $\Delta\varphi$ will not be precisely equal to zero. The nonzero closure phase cannot be due to some real signals as the phase variations due to real signals such as the genuine deformation or atmospheric delay inside a multilooking window are generally small and does not result in inconsistent phases. This nonzero term is because the filtering adds a term to each interferogram, the aim of which is reduce the noise term, which does not cancel in the closure phase calculation. This is not an issue for applications provided that the expected value of

* Corresponding author.

E-mail address: y.maghsoudi@leeds.ac.uk (Y. Maghsoudi).

<https://doi.org/10.1016/j.rse.2022.113022>

Received 16 August 2021; Received in revised form 18 March 2022; Accepted 26 March 2022

Available online 4 April 2022

0034-4257/Crown Copyright © 2022 Published by Elsevier Inc. This is an open access article under the CC BY license (<http://creativecommons.org/licenses/by/4.0/>).

this term is zero. However, De Zan et al. (2015) showed that the expected value of the filtering term is non-zero for some ground cover types.

Nonzero closure phases are a product of the spatial filtering and are mainly associated with the scattering and electrical properties of the ground surface (De Zan et al., 2015; Michaelides et al., 2019). Previous studies have suggested that changes in soil moisture and in the water content of vegetation might lead to these phase inconsistencies (De Zan and Gomba, 2018; De Zan et al., 2014). Although the amount of the bias caused by such inconsistencies is small in each individual interferogram, its accumulation in time can significantly impact the final estimated velocities, particularly for applications where millimetric accuracy is required. Ansari et al. (2021) showed short-interval multilooked interferograms are more impacted by this phenomenon and referred to this effect as the fading signal due to its short-lived nature. This is particularly problematic for time-series analysis approaches that exploit pixels where coherence can only be maintained for short time intervals – these pixels are likely to be strongly impacted by phase bias.

Mitigation strategies that have been proposed include correcting interferograms using physical models such as a moisture-induced phase model (De Zan and Gomba, 2018) or using “phase linking” (PL) approaches, described below. Due to the varied sources of the phase bias, employing a single physical moisture-induced phase model cannot account for all possible sources of phase inconsistencies and no generic model exists to incorporate all possible sources of the phase bias (Ansari et al., 2021). PL approaches, on the other hand, can effectively mitigate this phenomenon by incorporating all possible $N(N - 1)/2$ interferometric phases obtained from N SAR acquisitions (Guarnieri and Tebaldini, 2008). The key step in the PL approaches is to optimally estimate single-master phases for each pixel from all possible interferometric combinations. These methods retrieve maximum available information in InSAR data stacks (Samiei-Esfahany et al., 2016). Though efficient and robust, PL approaches require a large number of interferograms and are computationally expensive, particularly for systems like Sentinel-1, where there might be several hundred acquisitions. Moreover, the quality of the PL estimated phases highly depends on the availability of the long-term interferograms. In case of the decorrelated regions, the applicability and practicality of PL methods is limited. (De Luca et al., 2021) outlined a framework that did not show any significant bias. They showed that while exploiting networks of small baseline interferograms with also relatively high temporal baselines and including the processing stage discussed in (Pepe et al., 2015), which is an adaptation of the phase linking approach to the small baseline subset (SBAS) context using an efficient interferograms selection, the phase bias is not visible. This framework was tested on a set of high-coherent SAR pixels. Further investigation is needed to check the validity for lower coherence regions where the long-term coherence is difficult to maintain.

In this contribution, we first explore the characteristics of the phase bias by investigating its temporal and spatial behavior. We then develop and test an empirical mitigation strategy to correct short-term interferograms for the phase bias. Correcting for the phase bias in the short-term interferograms is of great importance, in particular when the small baseline algorithms e.g. (Berardino et al., 2002; Morishita et al., 2020) are being used.

Our approach assumes that there is a linear relationship between the bias in a single interferogram and the sum of the biases in the shorter interferograms spanning the same time. Employing this assumption, we can estimate bias corrections for each interferogram through a linear least squares inversion. We demonstrate the effectiveness of the proposed mitigation strategy by comparing the resultant velocities with the phase linking approach inversion.

2. Study site

We chose a study area in the west of Turkey that has a variety of ground cover types, including forested and agricultural areas where

long-term coherence is difficult to maintain (Fig. 1). Spatial heterogeneity in the land cover allows us to investigate the bias effect in these different land covers ranging from more coherent urban areas to the agricultural and forest areas. The area is imaged by Sentinel-1 A and B data on every overpass. We processed all interferometric pairs from one-year of Sentinel-1 acquisitions on track 36, where 60 images were acquired in the period spanning 1 February 2017 to 31 January 2018. All interferograms were generated using the automated workflows from the COMET-LiCSAR system (Lazecký et al., 2020), and were multilooked by factors of 5 in the range and 20 in the azimuth directions and geocoded onto a 100 m grid using elevation data from the Shuttle Radar Topography Mission (Farr et al., 2007).

3. Phase bias characterization

Although the bias in individual interferograms cannot be isolated, we can measure phase bias in sets of interferograms by examining loop closure phases using different combinations of data. Fig. 2 shows how we calculate the closure phase using a set of multilooked interferograms in a loop. In this example, we subtracted the sum of three 6-day interferograms (b), (c) and (d) from an 18-day interferogram (a) to isolate the loop closure phase (e). We use the notation

$\Delta\varphi^{18-6} = 18 \text{ day} - \sum_1^3(6 \text{ day})$ to denote this loop closure phase. For the rest of this paper $\Delta\varphi^{n-m}$ indicates the loop closure phase from subtracting the summation of all m day interferograms from an n -day interferogram spanning the same time. We also use the notation $\sum_{360 \text{ days}} \Delta\varphi^{n-m}$, for example, to show the 360-day cumulative loop closure

phase calculated as the difference between the 360-day “daisy chain” sum of interferograms with length n -days and m -days, where each “daisy chain” sum is calculated by adding successive n - or m -day interferograms with the secondary image in one interferogram becoming the primary image in the next. It should be noted that the closure phase values is assumed to be less than π in the absence of noise. We examined the validity of this assumption by checking the histograms of the long loops such as $\Delta\varphi^{360-6}$ and found out that, in our dataset, except for a small fraction of the pixels (<0.5%) the value is less than π (see Supplementary Fig. S1 in Supplementary material).

We use wrapped phases throughout this study to calculate the closure phases, with the result of any phase differences rewrapped to the interval $\pm\pi$. Taking a closer look at Fig. 2(e), we can see a spatially correlated signal that varies across the image.

To understand how the phase bias varies in interferograms of different lengths, we calculated the 360-day cumulative loop closure phase using $n = 60$ and $m = 6, 12, 18, 24, 30$ and 36 . The results are shown in Fig. 3(top).

The results show that shorter interferograms are more affected by this phenomenon, with cumulative loop closure phases reducing in size dramatically as the length of the shorter interferograms in the loop increases. This observation agrees with the effect of the fading signal (Ansari et al., 2021). The magnitude of the bias averaged over multiple pixels strongly depends on the ground cover type, with cropland and forested pixels having significantly larger bias than urban pixels (Fig. 3 (bottom)).

To test how the phase bias accumulates in time, we calculated $\sum_{i=1}^t (\Delta\varphi^{18-6})_i$ for $t = 1, \dots, 20$, 20 being the total number of consecutive 18-day interferograms in the 360-day observation period (Fig. 4). The results show that although the amount of the closure phase is small in each individual loop, it increases with time. The rate of bias accumulation is not steady throughout the year, being highest for cropland and lowest for urban pixels.

We also investigated the temporal variation in bias accumulation by calculating $\Delta\varphi^{60-6}$ and $\Delta\varphi^{60-12}$ loop closure phases (Fig. 5). Each plot in the first two rows of Fig. 5 belongs to a two-month period. Fig. 5 (bottom) illustrates the mean values for the total areas and also for different

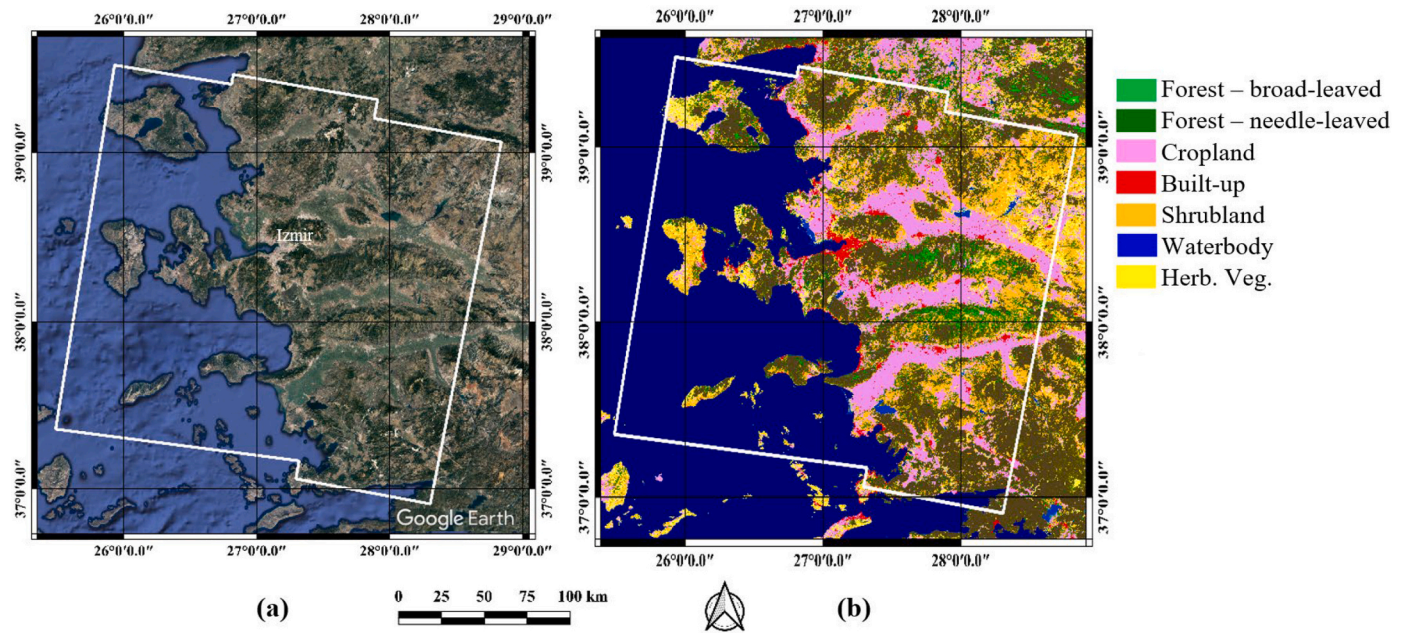


Fig. 1. Study site: (a) Overview of the study area located in the western Turkey. Izmir is the major city, situated along the Aegean coast. The white polygon shows the footprint of the Sentinel-1 data from descending path 36. (b) Land cover map obtained through the Copernicus Land Monitoring Service (<https://lcviewer.vito.be>).

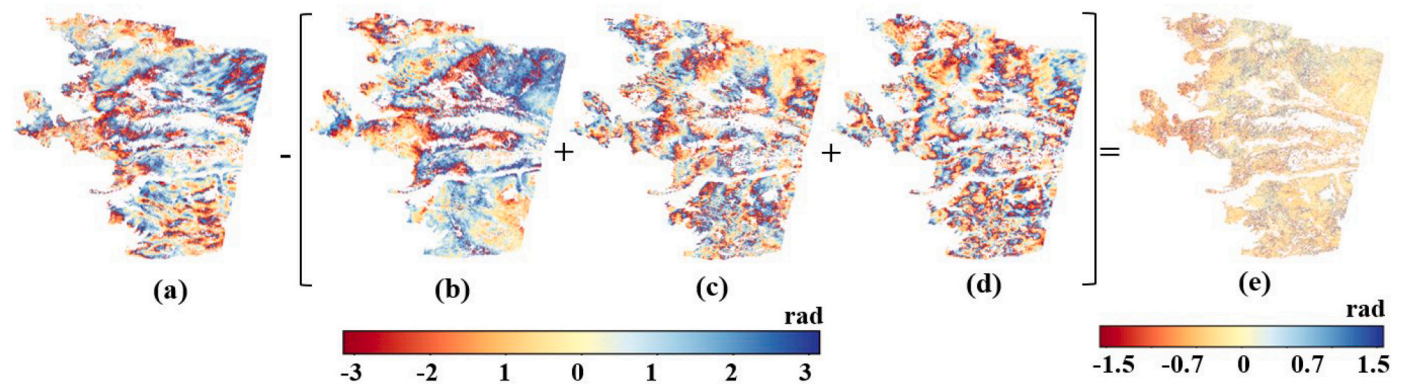


Fig. 2. Example of closure phase calculated from an 18-day interferogram and three 6-day interferograms. 18-day interferogram (a) spans 2017-02-18 to 2017-03-08. Three 6-day interferograms (b,c and d) span 2017-02-18 to 2017-02-24 (b), 2017-02-24 to 2017-03-02 (c) and 2017-03-02 to 2017-03-08 (d). The resulting closure phase is shown in (e).

landcovers. The plots indicate that the strength of the bias varies throughout the year. The largest mean value of phase bias is observed in the first plot, which corresponds to the period February and March.

The smallest mean value, on the other hand, occur in late summer (August to September). Comparing the values for $\Delta\varphi^{60-12}$ and $\Delta\varphi^{60-6}$, we see that they vary in a similar way, although as expected $\Delta\varphi^{60-12}$ is smaller, indicating that the ratio between them remains broadly constant (Fig. 5 bottom).

This matches well with the precipitation season in the west coast of Turkey (highest in January to March and lowest in July to September) as shown in Fig. 6. The closure phase in cropland pixels is more complex and may depend on several factors, including the vegetation growth as well as moisture variation.

Finally, in the last experiment of this section, we investigated the effect of the adaptive phase filtering (Goldstein and Werner, 1998) on phase bias. Phase filtering is commonly applied to interferograms to reduce phase noise which greatly improves phase unwrapping performance. We applied a spatial filter to the multilooked interferograms using an adaptive power spectrum filter with FFT window size = 32 and alpha = 1. Fig. 7 compares the cumulative loop closure phase

$\sum_{360 \text{ day}} (\Delta\varphi^{18-6})$ using unfiltered and filtered interferograms. Filtering increases the mean value of the loop closure phase (the bias), by effectively increasing the multilooking factor. Therefore, we recommend caution in using filtered interferograms for time-series analysis.

4. Phase bias correction

In the COMET-LiCSAR automatic processing system (Lazecký et al., 2020), interferograms have been processed that connect each epoch, i , to the three or four nearest acquisitions in time, backward and forward. We therefore aim to develop a bias correction approach that uses just the interferograms formed from the closest three connections so that accurate velocities can be obtained without requiring mass processing of large numbers of additional longer-term interferograms.

Several loop closure phases can be calculated for an individual pixel, from these interferograms, including:

$$\Delta\varphi_{i,i+2} = \varphi_{i,i+2} - (\varphi_{i,i+1} + \varphi_{i+1,i+2}) \text{ and} \quad (2)$$

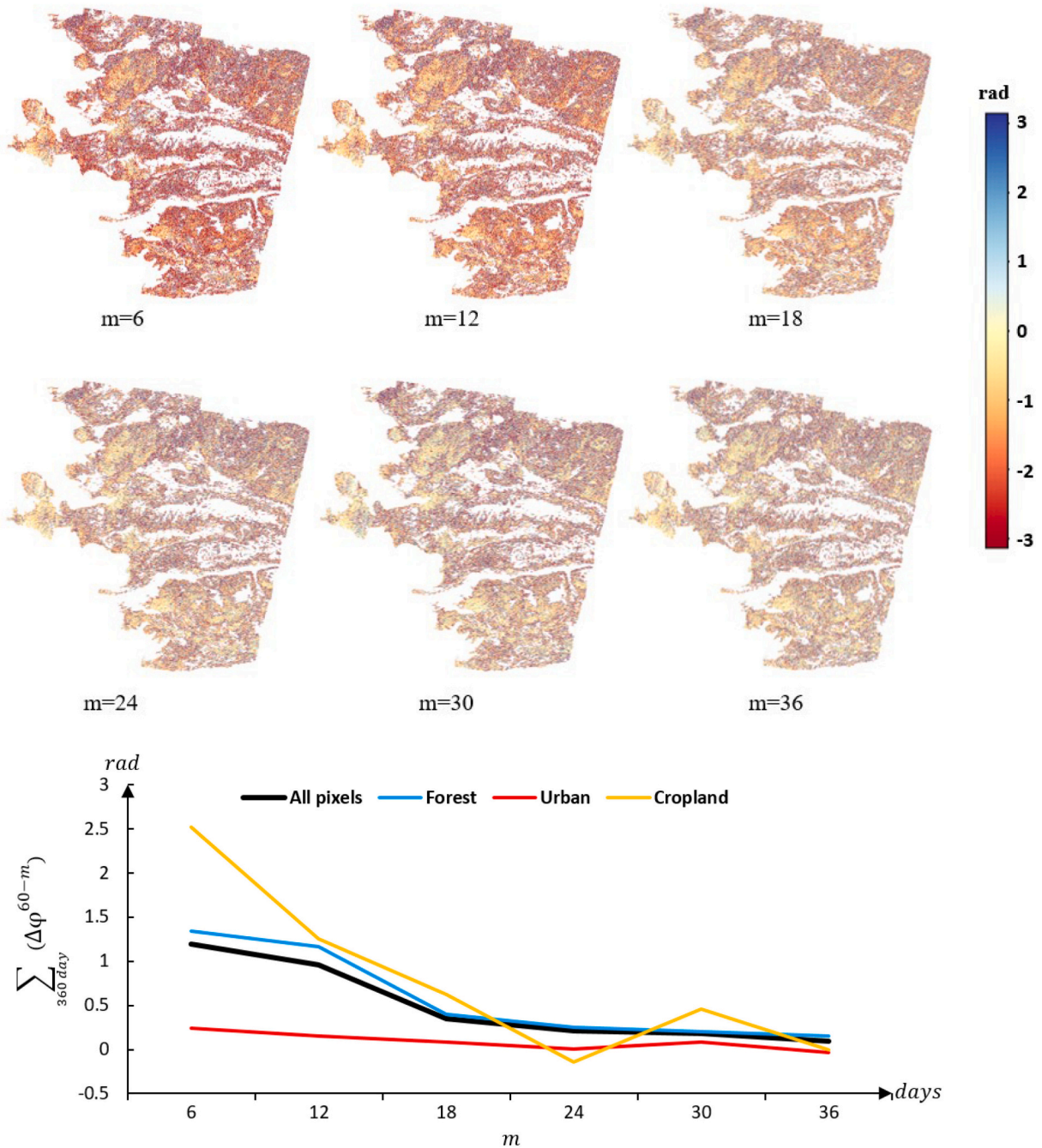


Fig. 3. 360-day cumulative loop closure phases, $\sum_{360 \text{ day}} (\Delta\varphi^{60-m})$, for varying timesteps, m (top), and mean value of cumulative loop closure phases for different land cover classes as a function of m (bottom).

$$\Delta\varphi_{i,i+3} = \varphi_{i,i+3} - (\varphi_{i,i+1} + \varphi_{i+1,i+2} + \varphi_{i+2,i+3}), \quad (3)$$

where $\Delta\varphi_{i,i+2}$ and $\Delta\varphi_{i,i+3}$ are the $\Delta\varphi^{12-6}$ and $\Delta\varphi^{18-6}$ loop closure phases respectively. Assuming the closure phase is due to biases and noise in each interferogram, Eq. (2) and (3) can be written as:

$$\Delta\varphi_{i,i+2} = \delta_{i,i+2} - (\delta_{i,i+1} + \delta_{i+1,i+2}) + \varepsilon \quad (4)$$

$$\Delta\varphi_{i,i+3} = \delta_{i,i+3} - (\delta_{i,i+1} + \delta_{i+1,i+2} + \delta_{i+2,i+3}) + \varepsilon, \quad (5)$$

where $\delta_{i,j}$ is the unknown phase bias in the interferogram formed from images i and j , and ε is the sum of the noise terms.

If we want to solve for the unknown phase bias terms $\delta_{i,j}$ on each 6-,

12- and 18-day interferogram, using the two sets of loop closure observations, $\Delta\varphi_{i,i+2}$ and $\Delta\varphi_{i,i+3}$, then with N acquisitions we have 2 $N-5$ observations and 3 $N-6$ unknowns. The system of equations is therefore underdetermined. (Michaelides et al., 2019) approached this problem by forming a set of closure phase equations as a function of the so-called “decorrelation phase”. The resulting matrix of observation equations is obviously a rank deficient. To solve this, they employed singular value decomposition (SVD) but this gives a solution that ignores any component of the real answer that lies in the null space.

In this study, we use the fact that, although the bias varies in time, we observe that it varies in a similar fashion for interferograms spanning different time intervals. This allows us to set up an overdetermined inverse problem, by introducing the assumption that the bias in an

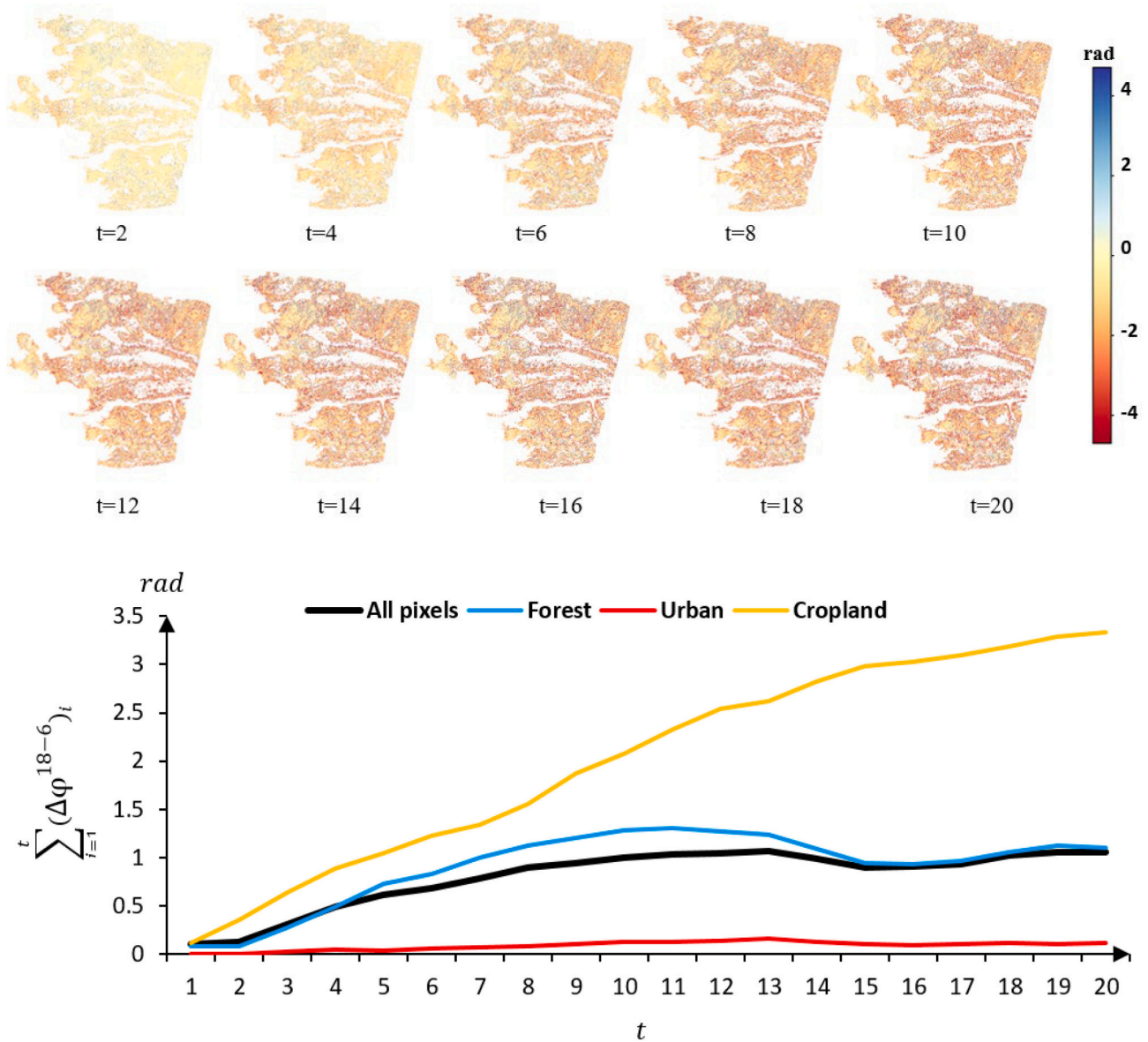


Fig. 4. The temporal accumulation of the loop closures obtained by $\sum_{i=1}^t (\Delta\varphi^{18-6})_i$ (top), and temporal accumulation of phase bias averaged for different land covers within the scene (bottom).

interferogram is linearly related to the sum of biases in shorter interferograms spanning the same time. In other words, although the bias varies in strength with time, we assume the change in strength of the bias in interferograms of different length is a constant ratio. i.e.

$$\delta_{i,i+2} = a_1 (\delta_{i,i+1} + \delta_{i+1,i+2}) \quad (6)$$

$$\delta_{i,i+3} = a_2 (\delta_{i,i+1} + \delta_{i+1,i+2} + \delta_{i+2,i+3}), \quad (7)$$

where a_1 and a_2 are unknown constants that linearly relate the bias in the longer interferograms to the sum of the corresponding biases in the short interferograms covering the same time period.

If we assume that 360-day interferograms have negligible bias, a_1 and a_2 can be estimated for each pixel by calculating the ratio of the cumulative loop closure phases for 12- and 6-day interferograms and 18- and 6-day interferograms respectively:

$$a_1 = \frac{\Delta\varphi^{360-12}}{\Delta\varphi^{360-6}} \quad \text{and} \quad (8)$$

$$a_2 = \frac{\Delta\varphi^{360-18}}{\Delta\varphi^{360-6}} \quad (9)$$

When estimating the regularization parameters a_1 and a_2 , only pixels that remain coherent for a period of 1 year can be used. Fig. 8 shows the maps of the a_1 and a_2 and their histograms. Although estimates of a_1 and a_2 for each pixel are noisy, there is no systematic pattern in space (Fig. 8 (top)), suggesting that a single value is appropriate. In this study, we used the mean values of 0.47 and 0.31 for a_1 and a_2 respectively for all pixels.

If a_1 and a_2 are constants, using Eqs. (4) to (7) and including all observations in epochs i to $i + 3$ leads to a series of observation equations relating the closure phases to unknowns $\delta_i, i+1$.

$$\begin{pmatrix} \Delta\varphi_{i,i+2} \\ \Delta\varphi_{i+1,i+3} \\ \Delta\varphi_{i,i+3} \end{pmatrix} \cong \begin{pmatrix} a_1 - 1 & a_1 - 1 & 0 \\ 0 & a_1 - 1 & a_1 - 1 \\ a_2 - 1 & a_2 - 1 & a_2 - 1 \end{pmatrix} \begin{pmatrix} \delta_{i,i+1} \\ \delta_{i+1,i+2} \\ \delta_{i+2,i+3} \end{pmatrix}. \quad (10)$$

This reduces the number of unknowns to $N-1$, the biases for the 6-day interferograms. The system of equations is then overdetermined when N

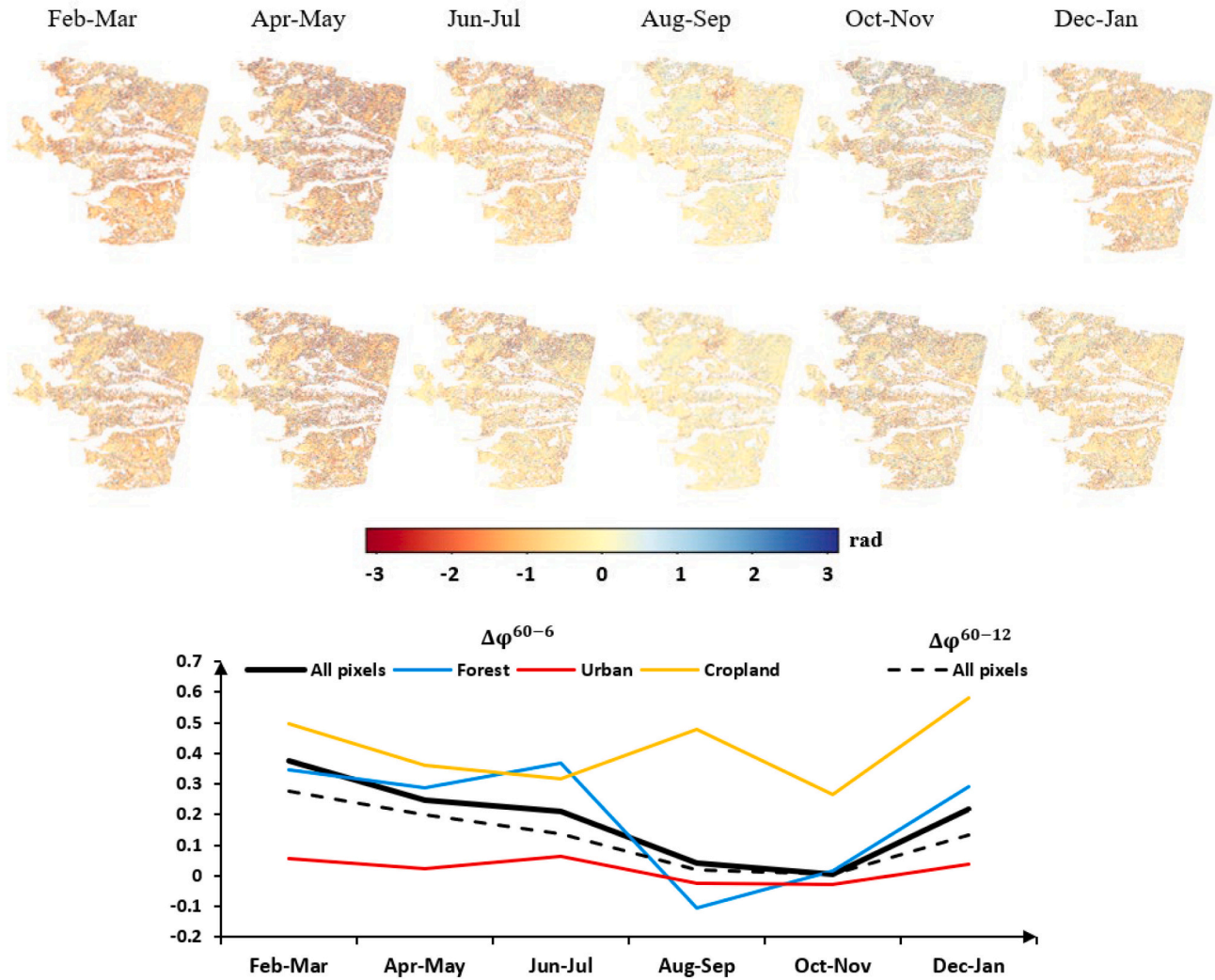


Fig. 5. Seasonal variation of the bias: the temporal plots of $\Delta\varphi^{60-6}$ (first row), $\Delta\varphi^{60-12}$ (second row) in 1 year, and mean value of $\Delta\varphi^{60-6}$ for different land cover classes (bottom panel). The mean values of $\Delta\varphi^{60-12}$ are plotted as a dashed line.

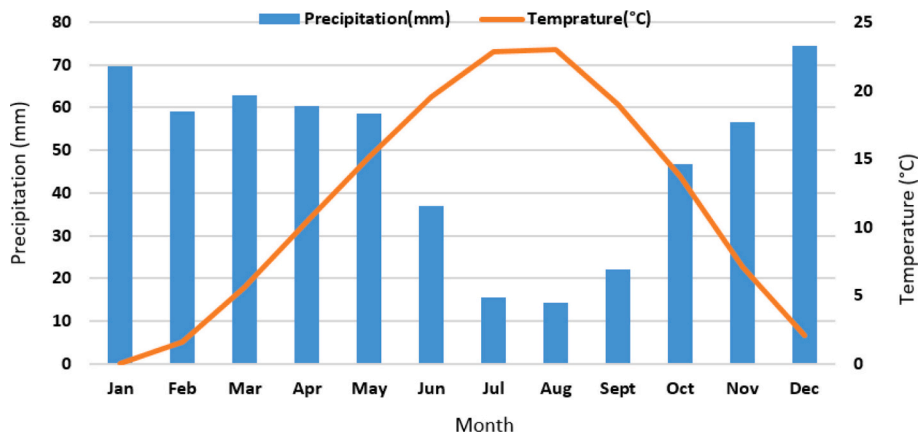


Fig. 6. Average monthly temperature and rainfall of Turkey for 1991–2020 obtained from <https://climateknowledgeportal.worldbank.org/country/turkey/climate-data-historical>

≥ 5 (with 2 N-5 loop closure observations) and the unknown bias terms can be estimated using a linear least squares inversion.

Upon the estimation of the bias terms, every single 6-, 12- and 18-day interferogram can then be corrected using

$$\varphi_{i,i+1}^c = \varphi_{i,i+1} - \hat{\delta}_{i,i+1} \quad (11)$$

$$\varphi_{i,i+2}^c = \varphi_{i,i+2} - \hat{\delta}_{i,i+2} = \varphi_{i,i+2} - a_1(\hat{\delta}_{i,i+1} + \hat{\delta}_{i+1,i+2}) \quad (12)$$

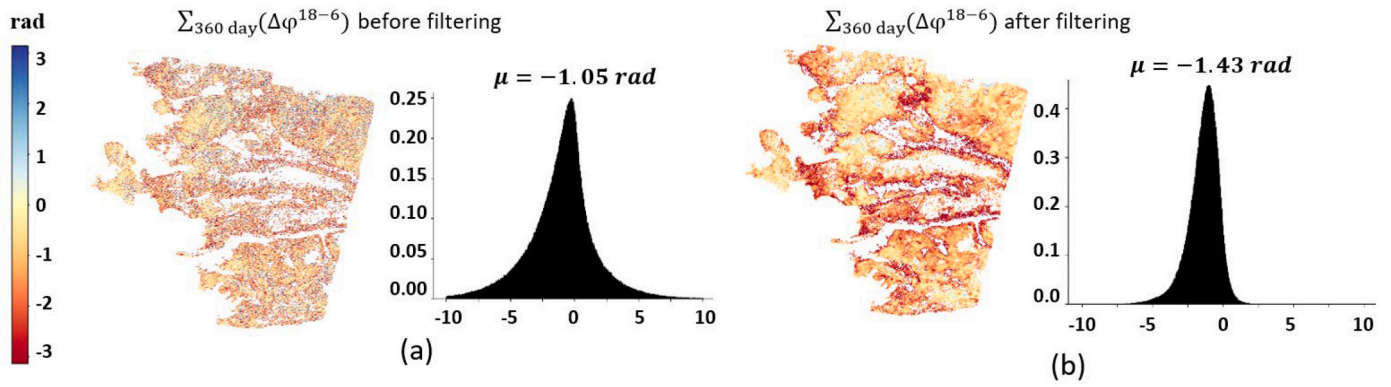


Fig. 7. $\sum_{360 \text{ day}} (\Delta\varphi^{18-6})$ and its histogram applied to the multilooked interferograms that are not filtered (a) and those that are (b). Here we used the adaptive Goldstein filtering.

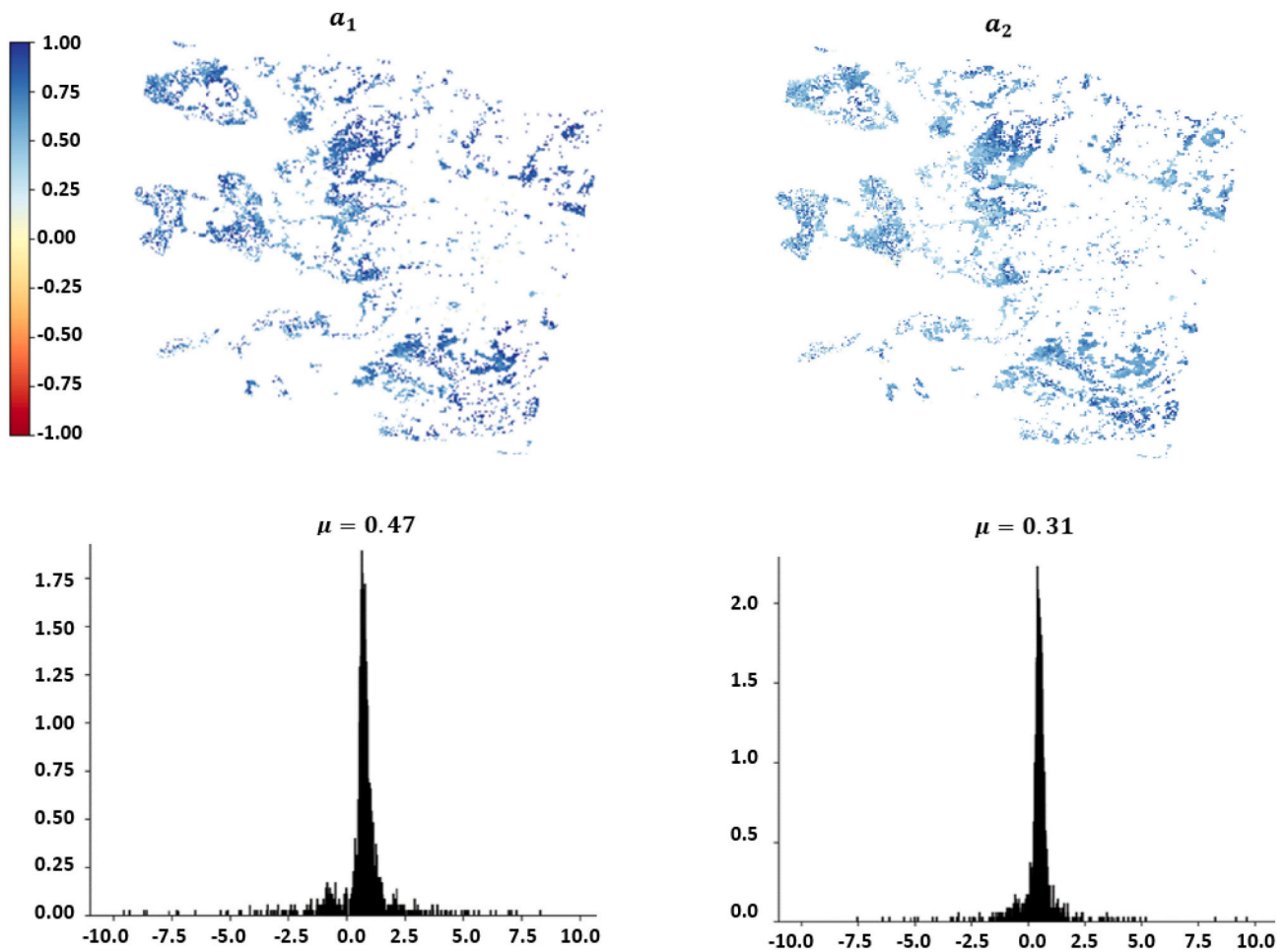


Fig. 8. Maps of a_1 and a_2 (top), and their corresponding histograms (bottom).

$$\varphi_{i,i+3}^c = \varphi_{i,i+3} - \hat{\delta}_{i,i+3} = \varphi_{i,i+3} - a_2(\hat{\delta}_{i,i+1} + \hat{\delta}_{i+1,i+2} + \hat{\delta}_{i+2,i+3}), \quad (13)$$

where $\varphi_{i, i+1}$, $\varphi_{i, i+2}$ and $\varphi_{i, i+3}$ are the original 6-day, 12-day and 18-day interferograms and $\varphi_{i, i+1}^c$, $\varphi_{i, i+2}^c$ and $\varphi_{i, i+3}^c$ are the corrected interferograms. The $\hat{\delta}_{ij}$ are the estimated bias terms. More in-depth investigation of a_1 and a_2 is in progress to gain more insight on their physical interpretation.

5. Correction results

All the experiments in this section were carried out on a set of coherent pixels, which were selected by applying a threshold of 0.3 on the 18-day average coherence. We estimated the corrections using Eq. (10) and corrected all the 6-day 12-day and 18-day interferograms covering our 360-day study period using Eqs. (11), (12) and (13) respectively.

Fig. 9 shows a comparison between the closure phase

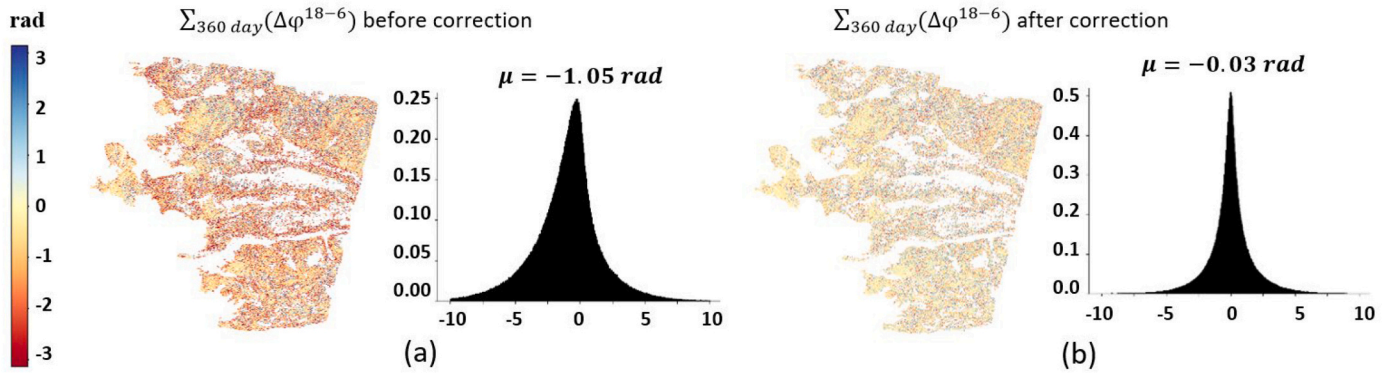


Fig. 9. The cumulative loop closure phase $\sum_{18 \text{ day} - 6 \text{ day}}^{18 \text{ day} - 6 \text{ day}} \Delta\varphi^{18-6}$ calculated using (a) the original interferograms (b) interferograms corrected with our empirical correction.

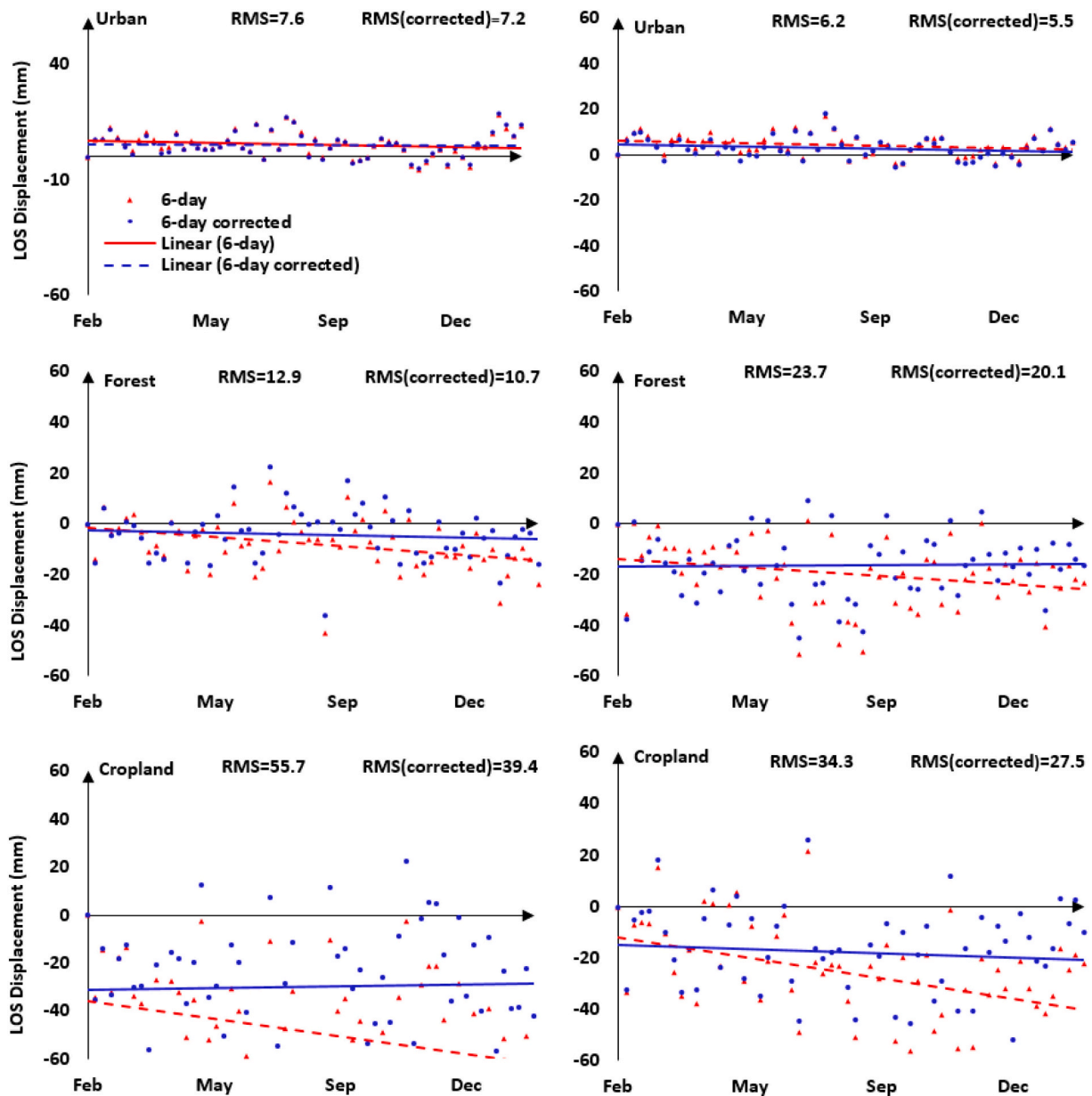


Fig. 10. The LOS time-series displacement for two example points in each land cover. RMS and RMS(corrected) show the root-mean-square of residuals calculated before and after correction respectively.

$\sum_{360 \text{ day}} (\Delta\varphi^{18-6})$ using the original interferograms and that found using the corrected interferograms. It is clear that correcting the interferograms has significantly decreased the closure phase, with its mean and the standard deviation decreasing from $-1.05 \pm 2.7 \text{ rad}$ prior to correction to $0.03 \pm 1.7 \text{ rad}$.

We also show (Fig. 10) corrected and uncorrected time series of line of sight (LOS) displacement calculated from just the 6-day interferograms for some example points in different land covers. Pixels in urban areas change the least with the correction, whereas the agricultural pixels have larger values of corrections. We also calculate the root-mean-square (RMS) of the residuals before and after the correction (Fig. 10); the correction reduces the scatter of the data for all land cover types. Considering all the pixels, the mean RMS residual of fit to the linear time series model has reduced from 27.2 rad before the bias correction to 20.7 rad after correcting for the phase bias.

In order to better understand the temporal variation of the estimated bias, we plotted the mean 6-day bias corrections, estimated from Eq. (10) for different land covers (Fig. 11). The bias is essentially zero for urban pixels throughout the year, whereas there is always a strong positive bias for cropland, which peaks in summer and has lowest values in winter, as we might expect if the physical cause is due to vegetation growth. The bias for forest is the most interesting, as it has positive values for most of the year, peaking in spring, but switches to negative values in autumn. This suggests a physical cause due to leaves growing on springtime and falling in the autumn. These curves are also consistent with the seasonal variation of the $\Delta\varphi^{60-6}$ and $\Delta\varphi^{60-12}$ shown in Fig. 5.

6. Validation

As well as demonstrating the reduction in cumulative loop closure phases, we can also compare line-of-sight velocities estimated from our corrected and uncorrected data with velocities from an approach that is less sensitive to phase bias. We use a Phase Linking (PL) approach for this validation test, which uses all possible interferograms and has been shown to be unaffected by phase bias of short-term interferograms (Ansari et al., 2021). There are a number of PL methods in the literature. These methods try to obtain the best estimates of $N - 1$ phase differences for a pixel relative to the primary date using the $N(N - 1)/2$ available interferometric phases. PL methods are categorized into maximum-likelihood estimators (Ferretti et al., 2011), least squares estimators (Samiei-Esfahany et al., 2016), Eigen decomposition-based phase estimators (Cao et al., 2016; Fornaro et al., 2015) and Eigen decomposition-based Maximum-likelihood estimator (Ansari et al., 2018).

Eigen decomposition-based methods are relatively computationally efficient and straightforward to implement; we use the approach from (De Zan et al., 2007; Fornaro et al., 2015), hereafter referred to as EPL, as our reference method to compare with results from our inversion that only uses short-interval interferograms.

$$T = \sum_{i=1}^N \lambda_i v_i v_i^H \quad (14)$$

where the eigenvalues λ_i are arranged in descending order as $\lambda_1 \geq \lambda_2 \geq \dots \geq \lambda_N$, v_i is the corresponding eigenvector associated with eigenvalue λ_i and H stands for the conjugate transpose. Phases $\hat{\varphi}$ are estimated by extracting the phases of the eigenvector associated with the largest eigenvalue. The EPL velocity i.e. V_{EPL} can then be estimated using these linked phases. Full details of the algorithm are described in (De Zan et al., 2007; Fornaro et al., 2015). We used the a posteriori coherence of (Ferretti et al., 2011) as a quality measure for phase estimation. The a posteriori coherence is a measure of goodness of fit between the PL estimated phases and the observed interferometric phases. In this study, we chose a value of 0.4 as a threshold for this measure to mask out the unreliable phases.

We calculated velocities from our corrected and uncorrected 6-day interferograms over the 360-day time period and checked the effectiveness of our bias correction strategy by comparing our estimated velocities before and after correction with the EPL velocities (Figs. 12, 13).

A scatterplot of the original 6-day estimated velocities for all pixels in our Turkey frame, $V_{6 \text{ day}}$, versus the velocities from EPL, V_{EPL} , is skewed to left (Fig. 12 (a)), indicating that the velocities for many of the pixels in the uncorrected 6-day velocities have a negative bias. By comparison, the scatterplot of the corrected 6-day velocities, $V_{6 \text{ day}}^c$, versus the V_{EPL} is centred on the diagonal 1:1 line (Fig. 12 (b)) indicating a high-degree of correlation between $V_{6 \text{ day}}^c$ and V_{EPL} and a dramatic reduction in the phase bias. The coefficient of determination, R^2 , increases from 0.19 before the correction to 0.63 after correction, and the RMSE decreased from 11.3 to 6.28 after correcting for the interferograms.

Plotting maps of the difference between velocities obtained with EPL and those calculated from our corrected/uncorrected 6-day interferograms (Fig. 13) confirms that the corrected velocities are much closer to those from EPL. Comparing the histograms shows that the mean and standard deviation of the differences between the velocities, changes from $-7.08 \pm 8.8 \text{ mm/yr}$, to $-0.28 \pm 6.2 \text{ mm/yr}$ after correction.

In the next experiment, we included all the 6, 12 and 18-day interferograms in our velocity estimation. We calculated velocities using both the original ($V_{6/12/18 \text{ day}}$) and the corrected interferograms ($V_{6/12/18 \text{ day}}^c$) and calculated their difference with V_{EPL} (Fig. 14). Using the corrected interferograms decreases the mean velocity bias to -0.1 mm/yr .

Similar to the velocity estimation using 6-day interferograms only, the scatterplot (Fig. 15) shows good correlation between EPL velocities and those estimated from 6/12/18-day interferograms, after correction. The coefficient of determination, R^2 , increases from 0.63 before the correction to 0.66 after correction, and the RMSE decreased from 6.4 to 6.0 after correcting for the interferograms.

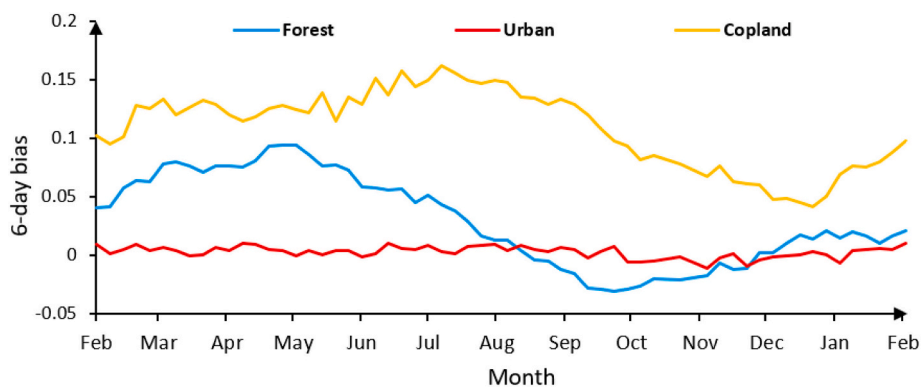


Fig. 11. Mean 6-day bias corrections obtained from Eq. (10) for different land covers.

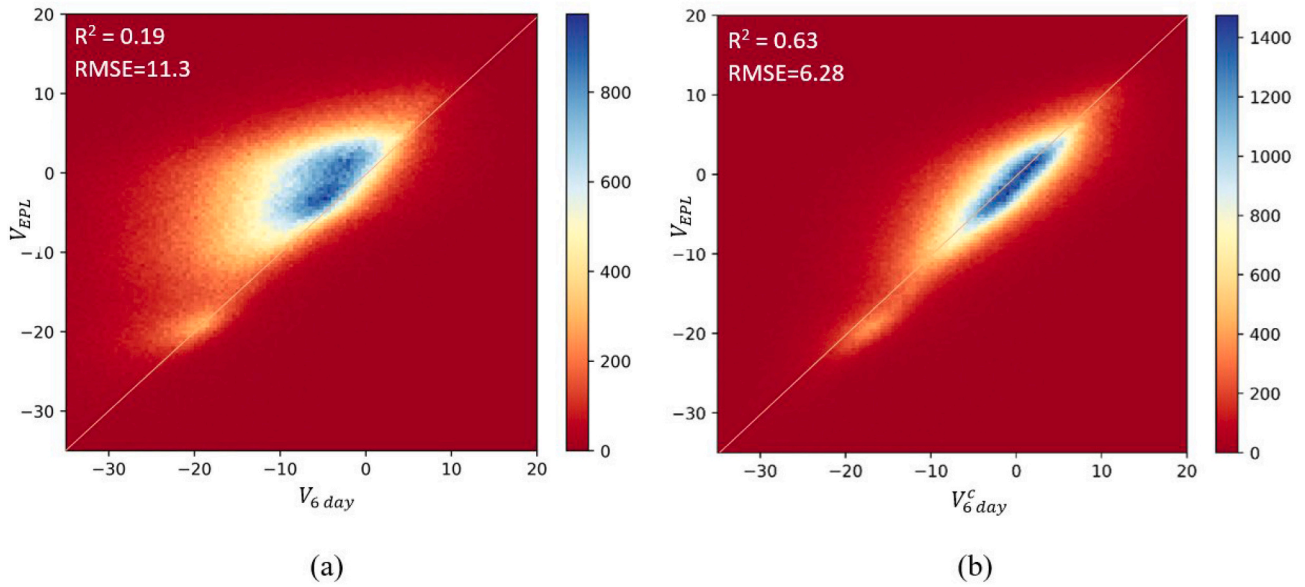


Fig. 12. Scatterplot of 360-day velocities obtained from Eigen decomposition Phase Linking (V_{EPL}) against velocities obtained from (a) uncorrected 6-day interferograms, $V_{6\text{ day}}$, and (b) 6-day interferograms corrected with our empirical approach $V_{6\text{ day}}^c$. Considering T as the N by N coherence matrix, the Eigen decomposition of T can be obtained as

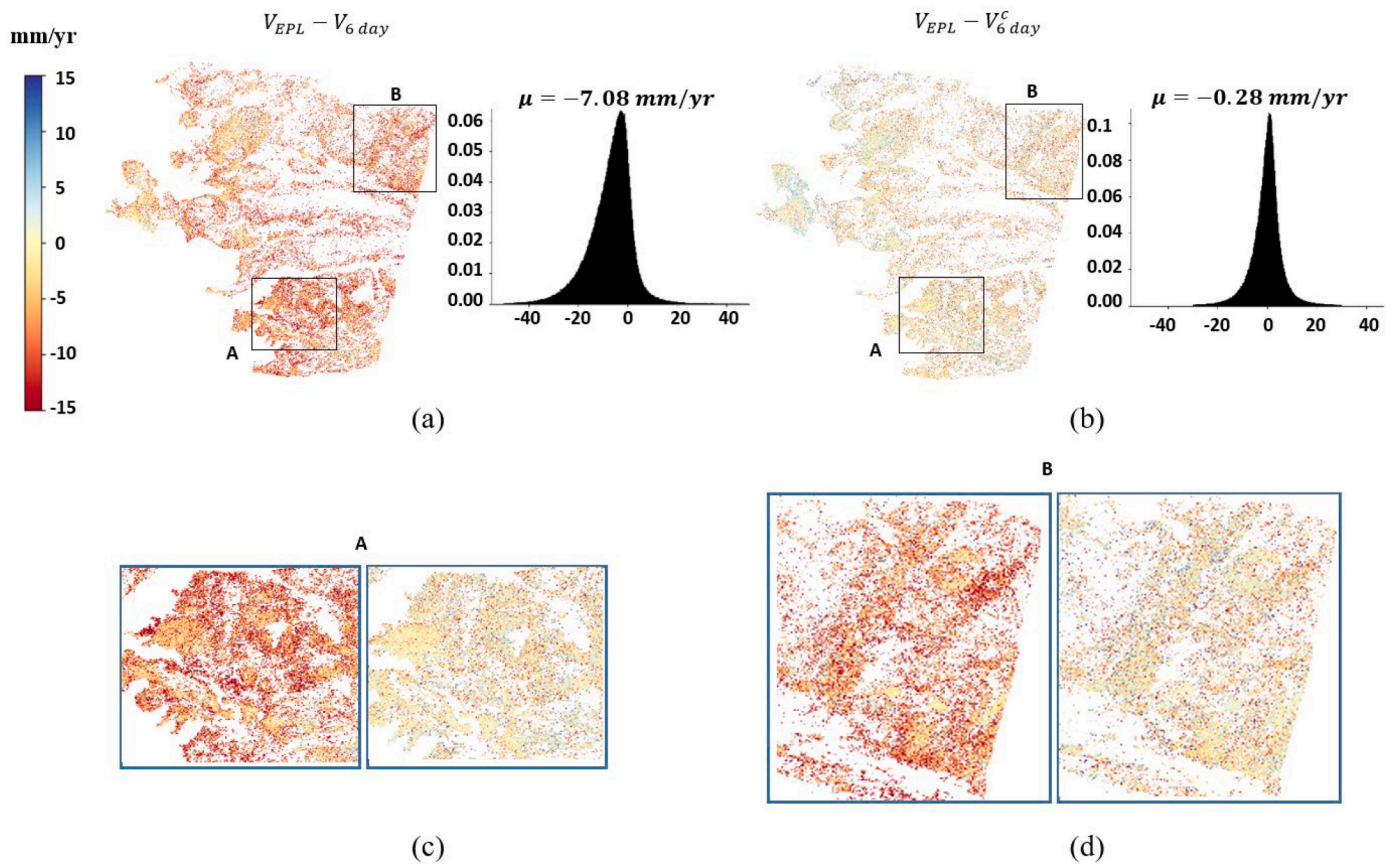


Fig. 13. Effect of the phase bias correction on the velocity estimation. Difference between the EPL velocity and (a) the uncorrected 6-day velocity i.e. $V_{EPL} - V_{6\text{ day}}$, (b) corrected 6-day velocity i.e. $V_{EPL} - V_{6\text{ day}}^c$ are shown as maps and histograms. (c,d) zoomed-in views of the two subsets for areas A and B.

Table 1 shows a summary of the average velocities obtained with the 6-day and 6/12/18-day interferograms before and after correction in different land cover classes. The EPL estimated velocities are also given in this table. For all land cover classes, our corrected velocities agree

well with those from phase linking approach. The remaining velocities observed for all techniques may be contaminated by residual atmospheric noise (our time series only covers 1 year), but also likely reflects genuine ground motion – agricultural areas in many parts of Turkey

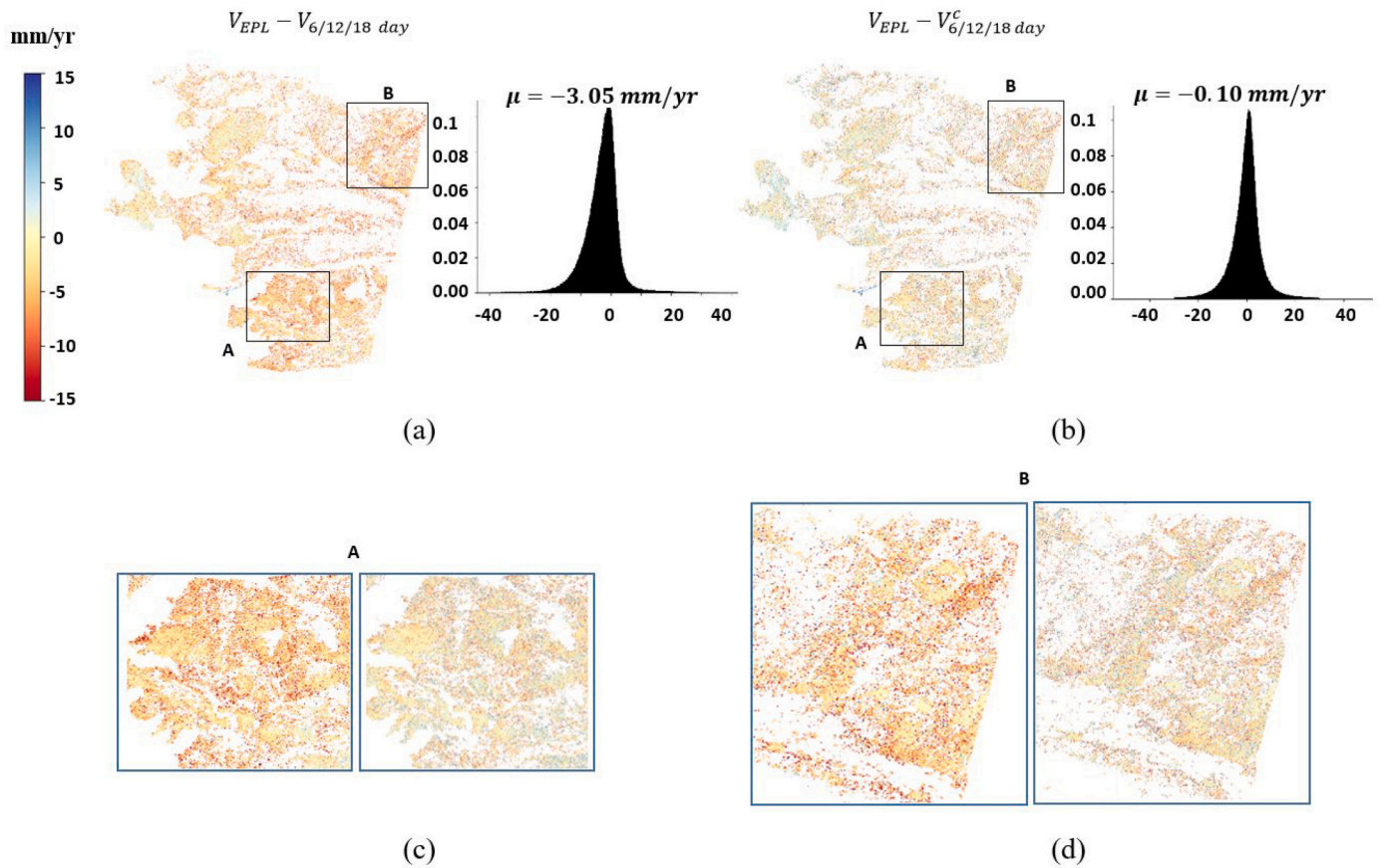


Fig. 14. The effect of the phase bias correction on the velocity estimation. $V_{EPL} - V_{6/12/18 \text{ day}}$ is shown in (a) and $V_{EPL} - V_{6/12/18 \text{ day}}^c$ is shown in (b). The zoomed-in view of the two subsets A and B are shown in panels (c) and (d) respectively.

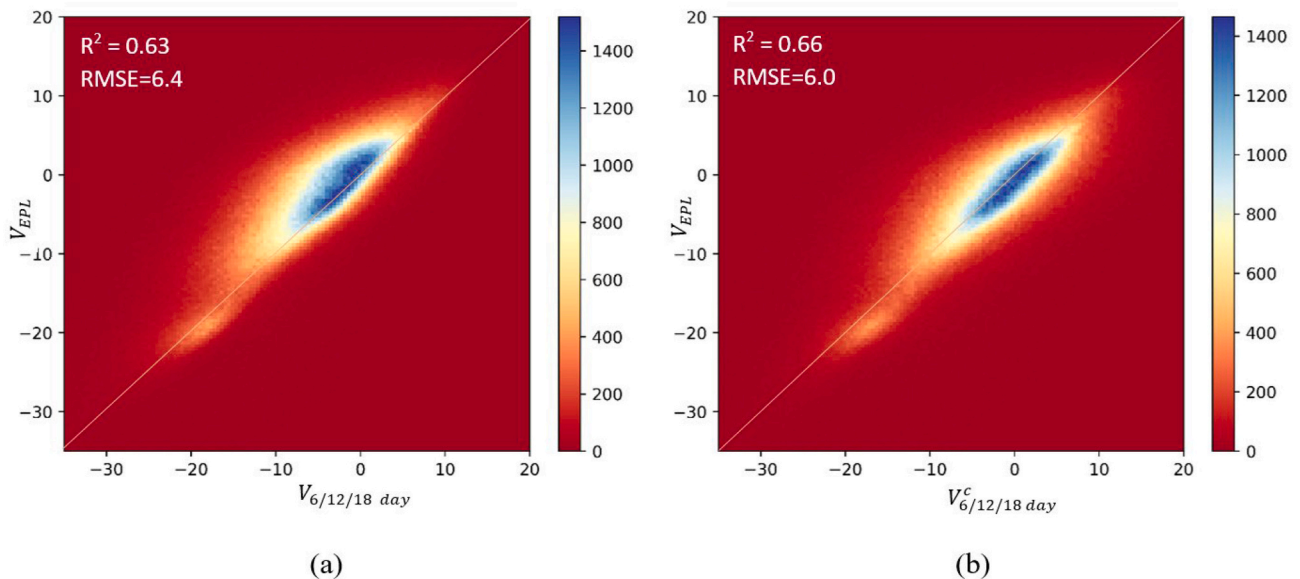


Fig. 15. Scatterplot of 360-day velocities obtained from Eigendecomposition Phase Linking (V_{EPL}) against velocities obtained from (a) uncorrected 6/12/18-day interferograms, $V_{6/12/18 \text{ day}}$, and (b) 6/12/18-day interferograms corrected with our empirical approach $V_{6/12/18 \text{ day}}^c$.

suffer from subsidence due to water extraction (Orhan, 2021).

Comparing Figs. 13 and 14 reveals that correcting the interferograms using the proposed strategy led to consistent phases. Upon correcting for the phase bias using the proposed method, it does not make any significant difference which stack of the interferograms be used for velocity

estimation and the 6-day velocity will have very similar performance as the 6, 12 and 18-day velocity. This demonstrates the consistency of the proposed strategy for correcting the phase bias.

Table 1

Summary of the average velocities in *mm/yr* obtained for all pixels and in different land covers

	All	Urban	Forest	Cropland
$V_{6 \text{ day}}$	10.8	7.1	15.0	40.2
$V_{6 \text{ day}}^c$	4.0	3.5	4.5	12.8
$V_{6/12/18 \text{ day}}$	6.7	5.0	8.8	21.1
$V_{6/12/18 \text{ day}}^c$	3.8	3.5	4.3	9.2
V_{EPL}	3.7	4.7	4.2	11.0

7. Conclusions

We have confirmed that short-interval interferograms can be highly affected by a phase bias, and its accumulation in time can highly impact estimated velocities. We provide a readily applicable method to estimate the bias corrections using only short interval interferograms. Our proposed correction strategy is simple and effective in addressing the phase bias and leads to velocities that compare well to the phase linking approach. The method relies on the estimation of two constant regularization parameters, which can easily be calculated using a single long-term interferogram. The proposed method is based on the assumption that the phase bias in an interferogram is linearly related to the sum of the bias shorter interferograms spanning the same time. This implies that, despite the decay of the average bias in time, the relative change in strength of the bias in interferograms of different length remains constant. This is entirely consistent with the bias exponential decay curve shown in (Ansari et al., 2021); this will be true as long as the decay time remains constant and only the magnitude of the bias changes. In this study, we used constant values for a_1 and a_2 , which relate the biases in 6-day interferograms with those in 12-day and 18-day interferograms. Further investigation is needed to determine if these are universal constants or if they vary spatially. Also, an in-depth and comprehensive investigation is needed to provide insight into the physical meaning of the constant values and whether they can be improved by other models/scenarios. We note that a similar approach could also be developed for areas where the revisit time for Sentinel-1 is 12 days.

Though efficient and robust, PL approaches are computationally expensive both in terms of generating $N(N - 1)/2$ interferograms and estimating the $(N - 1)$ optimal phases through often iterative optimizations of the underlying covariance matrix. However, our proposed method only requires calculating $(3N - 6)$ interferometric phases and solves for the bias correction through a single-step, straightforward and inexpensive least square inversion of Eq. (10). This is of high importance, particularly for automatic InSAR systems such as COMET-LiCSAR, which are designed to automatically produce InSAR products by processing all Sentinel-1 acquisitions in a frame (~ 60 new 6-day acquisitions per frame per year over Europe). The method can easily be adapted to allow larger number of connections. Given M as the number of connections per epoch, we have $\sum_{k=1}^M k \binom{N-1}{k} - k + 1$ observations and $N-1$ unknowns. Here, the constant values a_1, a_2, \dots, a_{M-1} can be calculated using the same procedure given in Eqs. (8) and (9). Additional research is needed to show that this works in practice.

More importantly, the quality of the PL estimated phases highly depends on the coherence of the long-term interferograms. In the case of the decorrelated regions such as forests or agricultural areas, where long-term coherence is difficult to maintain, the a posteriori coherence is degraded. Our proposed method, on the other hand, is less sensitive to this coherence loss as it only relies on the short term interferograms (6/12/18-day in this study) for estimating the correction terms. We identified a total of 2,400,000 points as coherent pixels, whereas this number decreased to 1,300,000 points when using the EPL approach. It should be noted that due to this limitation of the PL approach, we were only able to validate the proposed method over the coherent pixels (according to the a posteriori coherence). Yet, these pixels represents various land cover classes (forest, urban and cropland) and thus can be a

good representative set for the validation. Additional ground truth would be needed to expand the validation for all the pixels, but we note that velocities estimated for the non-coherent pixels are generally consistent with velocities for nearby validated coherent pixels. Our correction method can be applied to global compilations of short-term interferograms and offers the possibility of accurate long-term velocities without a requirement for coherence in long-term interferograms.

Supplementary data to this article can be found online at <https://doi.org/10.1016/j.rse.2022.113022>.

Acknowledgments, samples, and data

This research was supported by the Natural Environmental Research Council (NERC) through COMET. COMET is the UK Natural Environment Research Council's Centre for the Observation and Modelling of Earthquakes, Volcanoes and Tectonics, a partnership between UK Universities and the British Geological Survey. The Sentinel-1 data were obtained via the Copernicus Program of ESA and processed by the COMET-LiCSAR system. LiCSAR uses JASMIN, the UK's collaborative data analysis environment (<http://jasmin.ac.uk>).

CRedit authorship contribution statement

Yasser Maghsoudi: Conceptualization, Methodology, Software, Investigation, Writing – original draft, Visualization. **Andrew J. Hooper:** Conceptualization, Methodology, Writing – review & editing, Supervision. **Tim J. Wright:** Methodology, Writing – review & editing, Formal analysis, Supervision. **Milan Lazecky:** Resources. **Homa Ansari:** Validation.

Declaration of Competing Interest

The authors declare that they have no known competing financial interests or personal relationships that could have appeared to influence the work reported in this paper.

References

- Ansari, H., Zan, F.D., Bamler, R., 2018. Efficient phase estimation for interferogram stacks. *IEEE Trans. Geosci. Remote Sens.* 56, 4109–4125.
- Ansari, H., Zan, F.D., Parizzi, A., 2021. Study of systematic bias in measuring surface deformation with SAR interferometry. *IEEE Trans. Geosci. Remote Sens.* 59, 1285–1301.
- Berardino, P., Fornaro, G., Lanari, R., Sansosti, E., 2002. A new algorithm for surface deformation monitoring based on small baseline differential SAR interferograms. *IEEE Trans. Geosci. Remote Sens.* 40, 2375–2383.
- Biggs, J., Burgmann, R., Freymueller, J.T., Lu, Z., Parsons, B., Ryder, I., Schmalzle, G., Wright, T., 2009. The postseismic response to the 2002 M 7.9 Denali fault earthquake: constraints from InSAR 2003–2005. *Geophys. J. Int.* 176, 353–367.
- Cao, N., Lee, H., Jung, H.C., 2016. A phase-decomposition-based PSInSAR processing method. *IEEE Trans. Geosci. Remote Sens.* 54, 1074–1090.
- De Luca, C., Casu, F., Manunta, M., Onorato, G., Lanari, R., 2021. Comments on ``study of systematic bias in measuring surface deformation with SAR interferometry. *IEEE Trans. Geosci. Remote Sens.* 1–5.
- De Zan, F., Gamba, G., 2018. Vegetation and soil moisture inversion from SAR closure phases: first experiments and results. *Remote Sens. Environ.* 217, 562–572.
- De Zan, F., Rocca, F., Rucci, A., 2007. PS Processing with Decorrelating Targets.
- De Zan, F., Parizzi, A., Prats-Iraola, P., López-Dekker, P., 2014. A SAR interferometric model for soil moisture. *IEEE Trans. Geosci. Remote Sens.* 52, 418–425.
- De Zan, F., Zonno, M., López-Dekker, P., 2015. Phase inconsistencies and multiple scattering in SAR interferometry. *IEEE Trans. Geosci. Remote Sens.* 53, 6608–6616.
- Farr, T.G., Rosen, P.A., Caro, E., Crippen, R., Duren, R., Hensley, S., Kobrick, M., Paller, M., Rodriguez, E., Roth, L., Seal, D., Shaffer, S., Shimada, J., Umland, J., Werner, M., Oskin, M., Burbank, D., Alsdorf, D., 2007. The shuttle radar topography mission. *Rev. Geophys.* 45.
- Ferretti, A., Fumagalli, A., Novati, F., Prati, C., Rocca, F., Rucci, A., 2011. A new algorithm for processing interferometric data-stacks: SqueeSAR. *IEEE Trans. Geosci. Remote Sens.* 49, 3460–3470.
- Fornaro, G., Verde, S., Reale, D., Paucillo, A., 2015. CAESAR: an approach based on covariance matrix decomposition to improve multibaseline-multitemporal interferometric SAR processing. *IEEE Trans. Geosci. Remote Sens.* 53, 2050–2065.
- Foroughnia, F., Nemat, S., Maghsoudi, Y., Perissin, D., 2019. An iterative PS-InSAR method for the analysis of large spatio-temporal baseline data stacks for land subsidence estimation. *Int. J. Appl. Earth Obs. Geoinf.* 74, 248–258.

- Goldstein, R.M., Werner, C.L., 1998. Radar interferogram filtering for geophysical applications. *Geophys. Res. Lett.* 25, 4035–4038.
- Guarnieri, A.M., Tebaldini, S., 2008. On the exploitation of target statistics for SAR interferometry applications. *IEEE Trans. Geosci. Remote Sens.* 46, 3436–3443.
- Juncu, D., Árnadóttir, T., Hooper, A., Gunnarsson, G., 2017. Anthropogenic and natural ground deformation in the Hengill geothermal area, Iceland. *J. Geophys. Res. Solid Earth* 122, 692–709.
- Lazecký, M., Spaans, K., González, P.J., Maghsoudi, Y., Morishita, Y., Albino, F., Elliott, J., Greenall, N., Hatton, E., Hooper, A., Juncu, D., McDougall, A., Walters, R. J., Watson, C.S., Weiss, J.R., Wright, T.J., 2020. LiCSAR: an automatic InSAR tool for measuring and monitoring tectonic and volcanic activity. *Remote Sens.* 12.
- Massonnet, D., Briole, P., Arnaud, A., 1995. Deflation of Mount Etna monitored by spaceborne radar interferometry. *Nature* 375, 567–570.
- Michaelides, R.J., Zebker, H.A., Zheng, Y., 2019. An algorithm for estimating and correcting decorrelation phase from InSAR data using closure phase triplets. *IEEE Trans. Geosci. Remote Sens.* 57, 10390–10397.
- Morishita, Y., Lazecky, M., Wright, T.J., Weiss, J.R., Elliott, J.R., Hooper, A., 2020. LiCSBAS: an open-source InSAR time series analysis package integrated with the LiCSAR automated Sentinel-1 InSAR processor. *Remote Sens.* 12.
- Orhan, O., 2021. Monitoring of land subsidence due to excessive groundwater extraction using small baseline subset technique in Konya, Turkey. *Environ. Monit. Assess.* 193, 174.
- Pepe, A., Yang, Y., Manzo, M., Lanari, R., 2015. Improved EMCF-SBAS processing chain based on advanced techniques for the noise-filtering and selection of small baseline multi-look DInSAR interferograms. *IEEE Trans. Geosci. Remote Sens.* 53, 4394–4417.
- Samiei-Esfahany, S., Martins, J.E., Leijen, F.V., Hanssen, R.F., 2016. Phase estimation for distributed scatterers in InSAR stacks using integer least squares estimation. *IEEE Trans. Geosci. Remote Sens.* 54, 5671–5687.
- Temtime, T., Biggs, J., Lewi, E., Hamling, I., Wright, T., Ayele, A., 2018. Spatial and temporal patterns of deformation at the Tendaho geothermal prospect, Ethiopia. *J. Volcanol. Geotherm. Res.* 357, 56–67.
- Walters, R.J., Holley, R.J., Parsons, B., Wright, T.J., 2011. Interseismic strain accumulation across the North Anatolian fault from Envisat InSAR measurements. *Geophys. Res. Lett.* 38.
- Weiss, J.R., Walters, R.J., Morishita, Y., Wright, T.J., Lazecky, M., Wang, H., Hussain, E., Hooper, A.J., Elliott, J.R., Rollins, C., Yu, C., González, P.J., Spaans, K., Li, Z., Parsons, B., 2020. High-resolution surface velocities and strain for Anatolia from Sentinel-1 InSAR and GNSS data. *Geophys. Res. Lett.* 47 e2020GL087376.
- Zwieback, S., Liu, X., Antonova, S., Heim, B., Bartsch, A., Boike, J., Hajnsek, I., 2016. A statistical test of phase closure to detect influences on DInSAR deformation estimates besides displacements and decorrelation noise: two case studies in high-latitude regions. *IEEE Trans. Geosci. Remote Sens.* 54, 5588–5601.